Title
Tomography of dark-field scatter including single-exposure Moiré fringe analysis with X-ray biprism interferometry—A simulation study

Journal
Medical Physics, 48(10)

ISSN
0094-2405

Authors
Tao, Weijie
Sung, Yongjin
Kim, Sally Ji Who
et al.

Publication Date
2021-10-01

DOI
10.1002/mp.15134

Peer reviewed

Tomography of Dark Field Scatter Including Single-Exposure Moiré Fringe Analysis With X-ray Bi-prism Interferometry – A Simulation Study

Weijie Tao,[1,2] Yongjin Sung,[3] Sally Ji Who Kim,[4] Qiu Huang,[1] Grant T. Gullberg,[2] Youngho Seo,[2] Michael Fuller[5]

[1]Department of Nuclear Medicine, Rui Jin Hospital, School of Medicine, Shanghai Jiao Tong University, Shanghai, China; School of Biomedical Engineering, Shanghai Jiao Tong University, Shanghai, China

[2]Department of Radiology and Biomedical Imaging, University of California San Francisco, San Francisco, CA 94143-0946, USA

[3]Department of Biomedical and Mechanical Engineering, University of Wisconsin-Milwaukee, Milwaukee, WI 53211, USA

[4]Cardiovascular Research Center, Massachusetts General Hospital, Harvard Medical School, Boston, MA 02114, USA

[5]TF Instruments, Salinas, CA 93908, USA

Corresponding author: Grant T. Gullberg

Department of Radiology and Biomedical Imaging

University of California San Francisco, San Francisco, CA 94143-0946, USA

Email: gtgullberg@lbl.gov

Phone: (510) 525-1964

Keywords: X-ray phase contrast imaging, bi-prism interferometry, small angle scatter, dark field imaging

Running Title: X-ray Bi-prism Tomography

Abstract

Purpose: In this work we present tomographic simulations of a new hardware concept for X-ray phase-contrast interferometry wherein the phase gratings are replaced with an array of Fresnel bi-prisms, and Moiré fringe analysis is used instead of "phase stepping" popular with grating-based setups.

Methods: Projections of a phantom consisting of four layers of parallel carbon microfibers is simulated using wave optics representation of X-ray electromagnetic waves. Simulated projections of a phantom with preferential scatter perpendicular to the direction of the fibers are performed to analyze the extraction of small angle scatter from dark field projections for: 1) bi-prism interferometry using Moiré fringe analysis; 2) grating interferometry using phase stepping with 8 grating steps; and 3) grating interferometry using Moiré fringe analysis. Dark field projections are modeled as projections of voxel intensities represented by a fixed finite vector basis set of scattering directions. From the simulated projection data, an iterative MLEM algorithm reconstructs the coefficients of a fixed set of seven basis vectors at each voxel representing the small angle scatter distribution.

Results: Results of reconstructed vector coefficients are shown comparing the three simulated imaging models. The single-exposure Moiré fringe analysis shows increase in noise because of 1/8th the number of projection samples but also is obtained with less dose and faster acquisition times. Furthermore, replacing grating interferometry with bi-prism interferometry provides better CNR.

Conclusion: The simulations demonstrate the feasibility of the reconstruction of dark-field data acquired with a bi-prism interferometry system. With the potential of higher fringe visibility, bi-prism interferometry with Moiré fringe analysis might provide equal or better image quality to that of phase stepping methods with less imaging time and lower dose.

1. INTRODUCTION

Interferometry-based X-ray imaging has shown to provide excellent soft-tissue contrast of attenuation, phase, and small angle scatter. This requires developing imaging systems with highly resolved X-rays with fine, spatially-modulated intensity, which is feasible even with a conventional X-ray tube by using either a Talbot–Lau interferometer with diffraction gratings,[1] or an interferometer with refractive bi-prisms[2,3] in which there are no optics in the X-ray beam between the sample and the detector.[4] Accurately modelling the physics of these imaging systems are a vital part of advancing X-ray phase contrast tomography as it has been fundamental for the advancement of X-ray CT applications.

The first X-ray interferometer was built in the 1960s;[5] but it wasn't until 30 years later that the use of grating interferometry without X-ray lenses was first proposed by Clauser and Reinsch in 1992.[6] The first Talbot interferometer for hard X-rays was reported by Momose *et al*. in 2003.[7] Up until this time, Moiré patterns were used to extract the signal instead of phase stepping.[8-10] However, in 2005 Weitkamp *et al*.[11] introduced the phase stepping technique. Then in 2006 Pfeiffer *et al*.[12] was the first to use Talbot-Lau interferometry with gratings in combination with hard X-rays from an ordinary X-ray tube at a laboratory setup. Since then, significant advancements in hardware concepts and data processing methodology have advanced the technology of X-ray phase contrast imaging.

Our simulations investigate an X-ray interferometer (Fig. 1) wherein an array of Fresnel bi-prisms produces interference fringes with X-rays from a source grating (G_0). The source grating G_0 forms multiple mutually-incoherent sources of X-ray illumination. Rays from such a source thus formed refract through each element of a bi-prism and overlap as if proceeding from two slightly separated virtual sources of coherent rays. In our simulations, we rotate an analyzing grating G_2 to produce a Moiré pattern[13] with a period twice the resolution of the detector; much like previous gratings-based experiments. We compare the bi-prism interferometry system with the conventional grating system including a binary grating G_1 and phase stepping grating G_2; and a grating system with the same binary grading G_1 but the phase stepping grating G_2 is replaced with the same rotated grating G_2 used in the bi-prism simulations. In the simulations, the object to be imaged is rotated through the specified angles to capture tomographic angular views needed for reconstructing and analyzing the X-ray scattering resulting from the sample's internal microstructure.

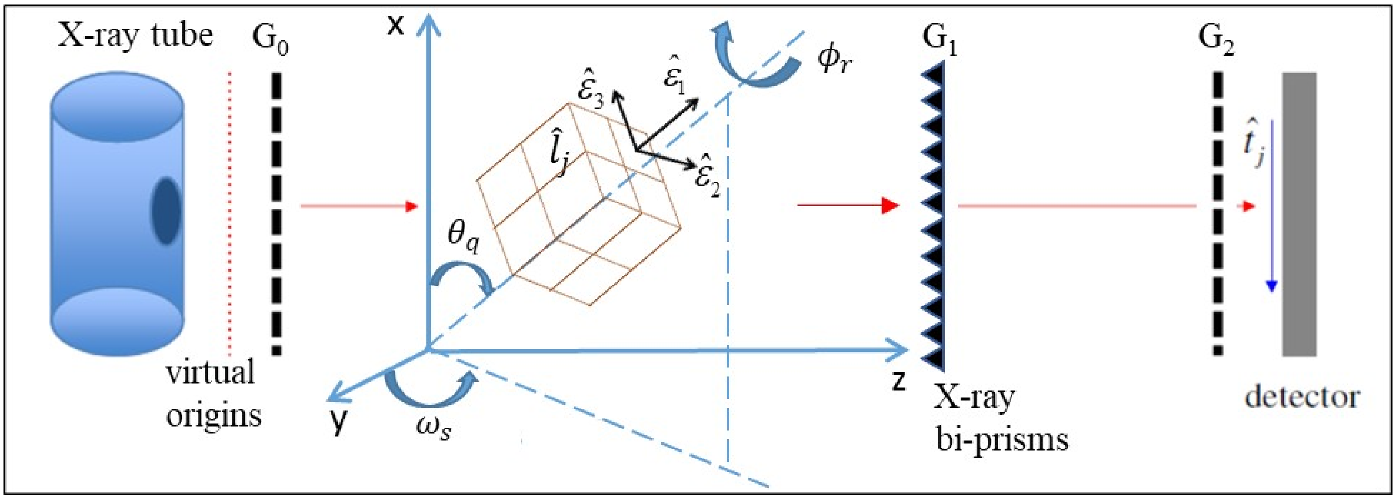

Fig. 1. Schematic diagram of the X-ray bi-prism interferometry system used in our simulations. An X-ray tube produces multiple X-rays passing through a source grating G_0. The source grating forms multiple coherent but mutually incoherent sources of X-rays. These refract or diffract through the G_1 grating (either bi-prism or binary grating in our simulations) and are scattered by the object. The resultant X-rays pass through an analyzing grating G_2 (either phase stepping grating or a rotated grating for Moiré fringe analysis in our simulations). In Section 2.B, we present the imaging model. For this model, the following unit vectors: $\hat{\epsilon}_1, \hat{\epsilon}_2, \hat{\epsilon}_3 \in R^3$ are scattering directions [in our simulations we used 7 scattering directions$(K=7)$], $\hat{l}_j \in R^3$ is the direction of the incoming X-ray beam, and $\hat{t}_j \in R^3$ is the sensitivity direction parallel to the detector surface.

The bi-prism is a different approach from gratings to produce refracted interference fringes for extracting the properties of X-ray interactions and is well suited for dark-field (small angle scatter) imaging of large areas. The bi-prism array interferometer provides spatially modulated intensity of a non-periodic visibility pattern (Fig. 2a), different from the Talbot interference pattern common with the use of gratings (Fig. 2b), across a wide field as each center fringe, thus produced, falls in a resonant position at the detector. An advantage is found in improved fringe visibility with broad X-ray spectra in that an X-ray bi-prism material has widely varied refracting power relative to wavelength and thus the separation of the virtual sources also varies with X-ray wavelength. Bi-prisms have had many applications in the optical regime.[2] Most of the investigations in X-ray bi-prism applications has been using hard X-rays generated in synchrotrons.[3,14-17] However, it has also found application to illustrate the wave-particle behaviour in the single-photon regime[18,19] and have also been used in interference electron microscopy.[20]

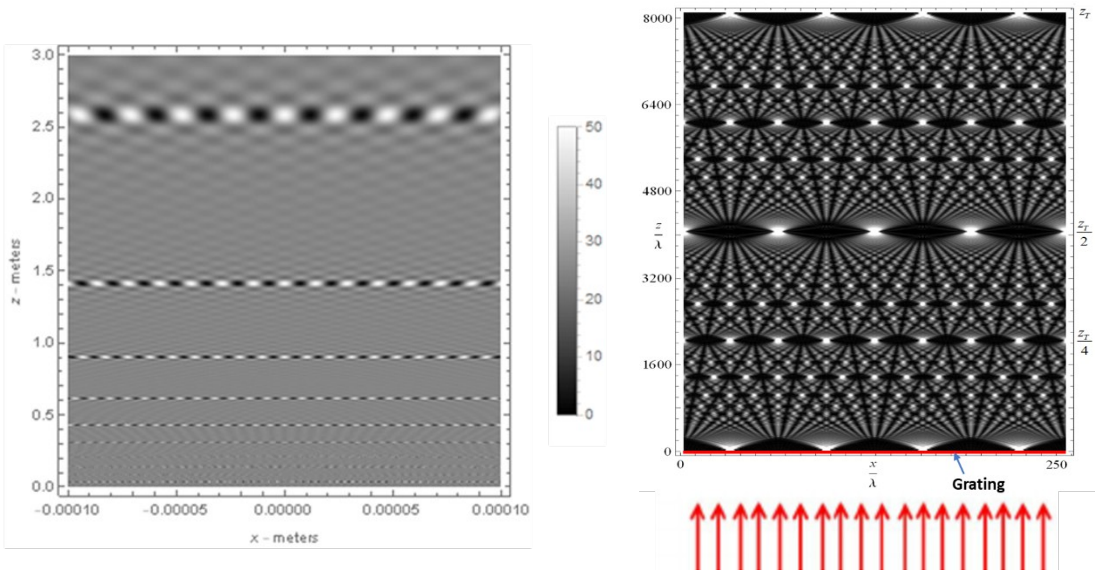

(a) (b)

Fig. 2. (a) Density plot of a fringe visibility pattern for 25-point sources with 1 bi-prism. The amplification of the interference pattern is repeated at non-periodic distances away from the plane of the bi-prism. For the calculation we set $\lambda = 7.1 \times 10^{-11}$m (17.5 keV), $I_p = 1/\Delta^2$, $\Delta = 7.00 \times 10^{-7}$, $\alpha = \delta \tan(\chi)$, $\delta = 1.57 \times 10^{-6}$ (silicon), $\chi = 82°$, $\eta = 0.4$ m, and $x_0 = 36.7\ \mu$m. (b) Talbot-Lau carpet. Illuminating plane wave passes through a grating producing a fringe pattern with replicating amplified fringe patterns at regular distances from the sources produced by the grating. At $z_T/2$ there is a secondary Talbot image and at z_T a replication of the original Talbot image that emerged from the grating. At $z_T/4$ there is a double frequency fractional image and increased frequency of images at less fractional distances. (Modified from Wikipedia: https://en.wikipedia.org/wiki/Talbot_effect.)

Until 2005, only Moiré fringe analysis produced by grating interferometry were used for extracting the properties of X-rays before mechanical phase stepping techniques.[7-10] Since then work has continued in the processing of Moiré fringe patterns through improved mathematics and Fourier analysis in combination with single shot scanning systems.[21-25] An interesting paper[10] used continuous wavelet transforms to extract the phase information from Moiré interferograms. A cost function is introduced for the adaptive selection of the ridge of the two-dimensional continuous wavelet transforms, and a dynamic programming algorithm is implemented to optimize the cost function. In other work[24] a two-dimensional checkerboard grating is placed at the first Talbot position beyond the object being imaged. Differential phase-contrast image and absorption image are obtained by Fourier analysis of Moiré fringe patterns generated by the grating on the X-ray detector. In two other papers,[23,25] three gratings: a source grating (G_0), phase grating (G_1), and analyzing grating (G_2), is used to produce a Moiré pattern for extraction of the phase information without phase stepping. In the one paper[23] a continuous helical sample rotation is implemented as routinely performed in clinical CT systems. The authors claim their proposed helical fringe-scanning procedure was the first to perform a phase-contrast CT scan with stationary gratings that delivers the complete sample information without any spatial interpolation. In our simulations we produce a Moiré pattern with a period twice the resolution of the detector by rotating an analyzing grating G_2; however, in our future design we propose to use a detector/scintillator with small hexagonal elements to provide the Moiré pattern.[26, 27]

In addition to hardware developments, significant advancements have been made in the development of algorithms for the reconstruction of phase contrast projections. In our work we use the model[28-31] developed by Pfeiffer's group for the projection of the small angle scatter. The model involves the reconstruction of coefficients of a fixed set of vector basis for each voxel which can be transformed to a tensor representation by fitting the vector basis to an ellipsoidal representation. (See Malecki thesis for an excellent description of the theory behind the model.[31]) The coefficients are reconstructed using an iterative MLEM algorithm. Iterative approaches have advantages in addition to modeling noise, to provide constraints on the solution. Investigations along this line were pursued by Brendel *et al.*[32] who proposed a cost function with regularization to iteratively reconstruct simultaneously attenuation, phase, and scatter images (with independent penalty functions) from differential phase contrast acquisitions, without the need of phase retrieval.

We use wave optics,[33,34] to simulate the absorption, phase, and scatter of X-rays through the object being imaged,[35-39] in evaluating our algorithm development for our bi-prism interferometry system. For the forward model, we use the scalar wave equation with the first-order Rytov approximation.[36] The bi-prism array generates straight interference fringes on the second grating, as a phase grating does in an existing grating-based system, with an additional advantage of modest chromatic aberration. Thus, we assume a monoenergetic source of X-rays and model the bi-prism array as a binary phase grating. The phase-modulated X-ray wave is propagated to the second grating using the angular-spectrum scalar wave theory.[33,34] The second grating is modeled as a binary amplitude grating, which is slightly rotated with respect to the bi-prism array to produce a Moiré fringe pattern. The raw image is generated after integration downsampling. Applying the Moiré fringe analysis to the raw image, we can extract the absorption, phase-contrast, and dark-field projection images. The calculation is repeated for different sample orientations, which provides the dataset for the tomographic reconstructions. In this particular work, we focus on the reconstruction of small angle scatter, but include the reconstruction of the linear attenuation coefficient, the phase, and the linear diffusion coefficient from the bi-prism simulated projections. The simulated projections of X-ray wave optics are reconstructed by modeling dark field projections of a finite set of fixed scattering directions at each voxel in space.[28-31]

In the sections that follow we present the Methods and Results in our simulation to evaluate bi-prism interferometry. In the Materials and Methods, we describe: a) a full wave approach with expressions of the refraction of X-rays passing through four layers of parallel carbon microfibers with preferential scattering perpendicular to the direction the fibers; b) a wave optics approach to the formation of grating and bi-prism dark field X-ray projections of small angle scatter; c) model of small angle scatter including a system matrix for forming projections of small angle scatter; d) processing the acquired phase stepping and Moiré projections; and e) reconstruction of X-ray attenuation, phase, small angle diffusion attenuation, and coefficients of small angle scatter basis functions. Results are presented for the reconstruction of coefficients for a basis of a set of fixed 7-vector directions - comparing reconstructions of dark field projections processed with phase stepping and Moiré fringe analysis. The results are followed by a discussion of the potential merits of bi-prism and phase stepping interferometry.

2. MATERIALS AND METHODS

2.A. Full wave approach to simulate X-ray phase contrast projections

In our previous paper,[4] we developed analytical expressions of the irradiance distribution pattern for a bi-prism interferometry system. This allowed us to study the non-periodic fringe pattern for various X-ray energies and for bi-prisms with various materials and dimensions. In the following subsections, we use wave optics to form X-ray phase contrast projections of a particular phantom designed to emphasize the dark field projections of small angle scatter.

2.A.1. Scalar wave function assuming first-ordered Rytov approximation

The scalar wave equation arrives from Maxwell's equation in free space for an electromagnet wave whose vector representation of the electric and magnetic disturbance can be represented by a scalar wave function with complex amplitude $\Psi(x, y; z)$.[33,34] (In the following we assume the square modulus is a reasonable approximation for the intensity of the irradiance distribution.). The scalar wave equation describes the interaction of X-rays with an object as a wave, and thus is appropriate to simulate the forward model for phase-sensitive X-ray imaging:

$$\left(\nabla^2 + k(\vec{r})^2\right)\Psi(\vec{r}) = 0 \quad ,$$

$$k(\vec{r}) = kn(\vec{r}),\ k = 2\pi/\lambda \quad ,$$

where λ is the wavelength in a vacuum and $n(x, y; z)$ is the complex refractive index of the object. Note that the refractive index decrement δ is related to the complex refractive index n: $n(x, y, z) = 1 - \delta(x, y, z) + i\beta(x, y, z)$, where $1 - \delta(x, y, z)$ and $\beta(x, y, z)$ is a measure of dispersion and of absorption, respectively.

Directly solving the wave equation, however, poses a great challenge because the wavelength is much smaller than the size of the object typically imaged with the technique. To address this challenge, the first-order Born or Rytov approximation has been adopted,[36] which greatly simplifies the solution for the scalar wave equation. The first-order Rytov approximation is more appropriate for X-ray imaging, because the imaged object is very thick (compared to the wavelength) but has a small refractive index difference (on the order of 10^{-7}). Using the first-order Rytov approximation, the complex amplitude $\Psi(x, y; z)$ of the X-ray wave function after the interaction with the object can be written as

$$\Psi(x, y; z) = \Psi_0(x, y; z) \exp[\phi_s(x, y; z)], \tag{1}$$

where $\Psi_0(x, y; z)$ is the X-ray's complex amplitude assuming no object in the beam path, and z is the distance from the center of the object. The complex scattered phase $\phi_s(x, y; z)$ can be related to the scattering potential of the object $Q(x, y; z)$ by

$$\tilde{\phi}_s(k_x, k_y; z) = [i 4\pi (k_z + 1/\lambda)]^{-1} \exp(i 2\pi k_z z) \tilde{Q}(k_x, k_y, k_z), \tag{2}$$

where λ is the wavelength in vacuum, k_z is determined by $k_z = \left((1/\lambda)^2 - k_x^{\,2} - k_y^{\,2}\right)^{1/2} - 1/\lambda$. $\tilde{\phi}_s(k_x, k_y; z)$ is the 2D Fourier transform of $\phi_s(x, y; z)$ with respect to x and y. $\tilde{Q}(k_x, k_y, k_z)$ is the 3D Fourier transform of $Q(x, y, z)$. The scattering potential $Q(x, y, z)$ is given by the complex-valued refractive index $n(x, y, z)$:

$$Q(x, y, z) = (2\pi/\lambda)^2 \left(1 - n(x, y, z)^2\right). \tag{3}$$

We note that the first-order Rytov approximation used for this derivation has been validated for absorption and phase calculation using the Mie solution, which is the exact solution for the Maxwell's equations.[36] In dark-field imaging, the image contrast originates from the unresolved, microscopic variations of refractive index in the sample.[40-42] Thus, for dark-field simulation, a forward model that can handle multiple scattering would be appropriate, e.g., multi-slice approaches using either the angular-spectrum scalar wave theory[43] or the beam-propagation method.[44] However, the multi-slice approaches require a voxelated phantom as an input, and thus are hard to be upscaled, because a grid size smaller than the microstructure (e.g., microfibers generating the anisotropic dark-field signal) in the sample would be required. In contrast, the forward model we adopt can include such a microstructure much more efficiently. For example, the complex scattered phase in Eq. (1), which is calculated by Eq. (2), is related to the Fourier transform of the scattering potential as an input. As we have shown in previous work,[37] we can calculate $\widetilde{Q}(k_x, k_y, k_z)$ for a numerical phantom defined with NURBS. The NURBS surface, defined on a 2D grid, can be refined much more efficiently than a 3D voxelated phantom.

2.A.2. Scalar wave function for X-rays interacting with a phantom of parallel carbon fibers

To evaluate our algorithms for the reconstruction of small angle scatter, we use a stack of microfibers as an object to be imaged (Fig. 3). Within the limit of the first-order approximation, the complex amplitude $\Psi(x, y; z)$ of X-rays after a stack of microfibers can be calculated as a sum of the complex amplitudes for individual microfibers. Similarly, $\widetilde{Q}(k_x, k_y, k_z)$ for the entire stack can be represented by a sum of $\widetilde{Q}_i(k_x, k_y, k_z)$ for the individual microfibers.

Each microfiber will have different lengths but same radius. Therefore, a homogeneous cylinder with length L_i, radius R, and refractive index n_0, which is oriented along the x direction, the scattering potential $Q_i(x, y, z)$ for one microfiber is

$$Q_i(x, y, z)=(2\pi/\lambda)^2\left[1-n_0^2\Pi\left(2\left[y^2+z^2\right]/R\right)\Pi\left(x/L_i\right)\right] \quad ,$$

where the rectangle function Π is defined as

$$\Pi(x)=\begin{cases} 1\, if -\frac{1}{2}<x<\frac{1}{2} \\ 0\, otherwise \end{cases}$$

The 3D Fourier transform of $Q_i(x, y, z)$ can be written as

$$\widetilde{Q}_i(k_x, k_y, k_z)=(Q_0 R\, L_i/\rho)J_1(2\pi R\rho)\, sinc(L_i k_x), \tag{4}$$

where $Q_0=(k_0)^2(1-n_0{}^2)$, $\rho=(k_y{}^2+k_z{}^2)^{1/2}$, $k_0=2\pi/\lambda, n_0$ is the complex index of refraction for each microfibers, J_1 is the Bessel function of the first kind of order 1, and $sinc(x)=\sin(x)/x$. Under the projection and paraxial approximations, the 2D Fourier transform of the complex scatter phase $\tilde{\phi}_{s_i}$ for one microfiber can be writer as

$$\tilde{\phi}_{s_i}(k_x, k_y; z) = \frac{\lambda}{i4\pi} \exp\left[-i\pi\lambda z\left(k_x^2 + k_y^2\right)\right] \tilde{Q}_i(k_x, k_y, 0).$$

Substituting for $\tilde{Q}_i(k_x, k_y, 0)$

$$\tilde{\phi}_{s_i}(k_x, k_y; z) = \frac{\lambda}{i4\pi} \exp\left[-i\pi\lambda z\left(k_x^2 + k_y^2\right)\right] \left(Q_0 R L_i / k_y\right) J_1(2\pi R k_y)\, sinc(L_i k_x),$$

where $\rho = k_y$. The Fourier transform of the total scattering potential $\tilde{Q}_t(k_x, k_y, k_z)$ is

$$\tilde{Q}_{s_t}(k_x, k_y, k_z) = \sum_{i=1}^{N_{fibers}} e^{-i2\pi(k_x x_i + k_y y_i + k_z z_i)} \left(Q_0 R L_i / \rho\right) J_1(2\pi R\rho)\, sinc(L_i k_x)$$

where N_{fibers} is the total number of fibers, which for our case N_{fibers} = 4×71,000 = 284,000.

Now the 2D Fourier transform of the complex scattered phase for all layers is

$$\tilde{\phi}_{s_t}(k_x, k_y; z) = \frac{\lambda}{i4\pi} \exp\left[-i\pi\lambda z\left(k_x^2 + k_y^2\right)\right] \tilde{Q}_t(k_x, k_y, 0).$$

Substituting for $\tilde{Q}_t(k_x, k_y, 0)$,

$$\tilde{\phi}_{s_t}(k_x, k_y; z) = \frac{\lambda}{i4\pi} \exp\left[-i\pi\lambda z\left(k_x^2 + k_y^2\right)\right] \sum_{i=1}^{N_{fibers}} e^{-i2\pi(k_x x_i + k_y y_i)} \left(Q_0 R L_i / k_y\right) J_1(2\pi R k_y)\, sinc(L_i k_x)\,.$$

Therefore, the complex amplitude $\Psi_1(x, y; z)$ of X-rays after a stack of microfibers is

$$\Psi_1(x, y; z) = \Psi_0(x, y; z) \exp\left[\phi_{s_t}(x, y; z)\right]. \tag{5}$$

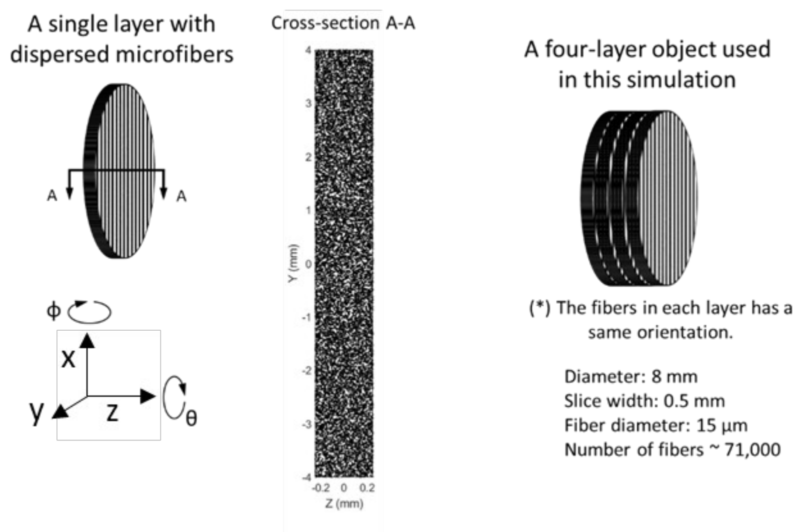

Fig. 3. Phantom used in the simulations. The phantom consisted of four layers of parallel carbon microfibers to provide preferential scatter perpendicular to the direction of the fibers. The angles ϕ and θ show the rotation directions of the projections of the phantom.

2.A.3. Simulation of X-ray propagation through gratings

In the following we follow the development in Sung *et al.*[39] to arrive at an expression for the intensity at the detector of the simulated projections of the phantom in Fig. 3. At a distance z from the phantom, the complex amplitude $\Psi_1(x,y;z)$ of X-rays in the transverse plane is given in Eq. (5).

Suppose that G_1 is located at a distance D_1 from the center of the object (Fig. 4). Then the complex amplitude right before the phase grating G_1 is $\Psi_1(x,y;D_1)$. The complex amplitude right after the phase grating G_1 is

$$\Psi_2(x,y)=\Psi_1(x,y;D_1)\exp\{i\Delta\phi[\Pi(x/p)*III(x/p)]\} \quad , \tag{6}$$

where $\Delta\phi$ can be π or $\pi/2$, p is the grating period, and $III(x)=\sum_{m=-\infty}^{m=\infty}\delta(x-m)$.

The propagation of X-rays between G_1 and G_2 can be calculated using the angular spectrum scalar wave theory.[34] The complex amplitude right before G_2 is

$$\Psi_3(x,y)=F_2^{-1}\{\tilde{\Psi}_2(u,v)H(u,v;D_2)\} \quad , \tag{7}$$

where D_2 is the distance between G_1 and G_2, F_2^{-1} is the 2D inverse Fourier transform, $\widetilde{\Psi}_2(u,v)$ is the 2D Fourier transform of $\Psi_2(x,y)$, and

$$H(u,v;D_2)=\exp\left\{i(2\pi/\lambda)D_2\left[1-(\lambda u)^2-(\lambda v)^2\right]^{1/2}\right\},$$

is the transfer function for the light-field propagation between G_1 and G_2.

The intensity before G_2 is $I_3(x,y)=|\Psi_3(x,y)|^2$ and the intensity at the n*th* step after a phase stepping grating G_2 of N steps is

$$I_4^{(n)}(x,y;n)=I_3(x,y)\left[\Pi\left(\frac{x}{p}\right)*III\left(x/p-\frac{n}{N}\right)\right]. \quad (8)$$

Assuming the camera has $N\times N$ square pixels $\Delta\times\Delta$, the intensity at the (i,j) pixel can be written as

$$I_5(i,j)=\int_{-\Delta/2}^{\Delta/2}\int_{-\Delta/2}^{\Delta/2} I_4^n(i\Delta+\xi,j\Delta+\eta)\,d\xi d\eta. \quad (9)$$

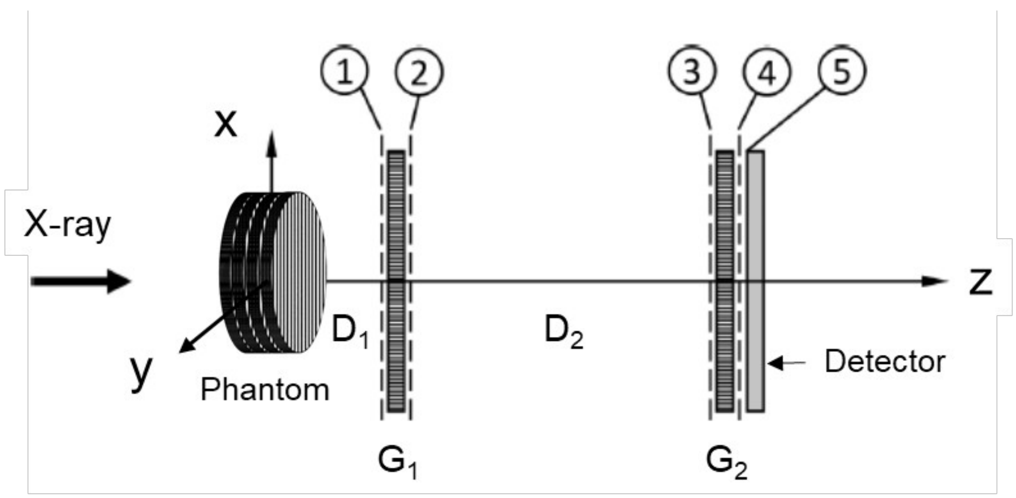

Fig. 4. Schematic diagram of the simulation geometry used in the simulation study. G_1 and G_2 are the gratings and the phantom is the four layers of fibers shown in Fig. 3. D_1 is the distance between the phantom and the first grating G_1. D_2 is the distance between the first grating and the second grating G_2. The numbers 1 through 5 in the circles refer to the planes where Eqs. (5)-(9) were calculated. For the phase grating simulation, the phase grating G_2 was shifted 8 positions in the y-direction over one period. For the Moiré simulation G_2 was rotated by 3°. (This figure was modified from Fig. 1 in Sung *et al.*[39])

2.A.4. Simulation of X-ray propagation through a bi-prism and a grating

In the previous case, the first grating G_1 was a binary grating. Suppose we want to replace the binary grating with a bi-prism for which the phase after the bi-prism can be represented by $e^{(i\phi(x))}$, where $\phi(x)$ is the projection of the bi-prism along the x-direction in Fig. 5. If we ignore scatter in the bi-prism material, the complex amplitude of the scalar wave function right after the bi-prism array G_1 is

$$\Psi_2(x,y)=\Psi_1(x,y;L)\exp\{i\Delta\phi[(\bigwedge(x/p)*\Pi(x/p))*III(x/p)]\} \quad , \tag{10}$$

where $\bigwedge(x)$ is the triangle function:

$$\bigwedge(x)=\begin{cases}1-|x|\, if\, |x|<1\\ 0\, if\, |x|>1\end{cases} \quad .$$

However, for our simulations of projections involving a bi-prism array, Eq. (10) was not used, but instead to reduce the computational cost, we used a binary phase mask with a period of 5 μm and a phase delay of $\phi(x)$. The phase delay of $\phi(x)$ was specified after the grating, which was equivalent to a bi-prism angle of 84.624°. No material property (refractive index and the thickness) needed to be specified.

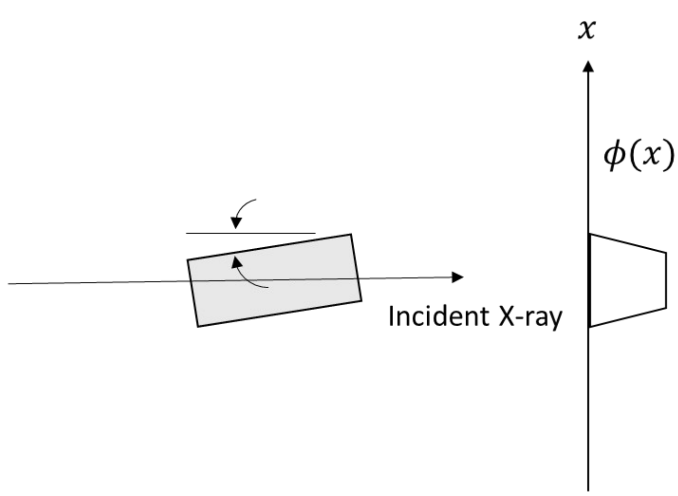

Fig. 5. Bi-prism replaces the binary grating in G_1 for the simulations. This results in a trapezoidal phase shift along the x-direction, which can be represented as $\phi(x)=\bigwedge(x)*\Pi(x)$.

•

2.B. Model of the projection of small angle scatter

Using the previous expression for the pixel intensities in Eq. (9) one comes up with the projection values of the intensity of the wave optics representation of the scatter potential. We show later that using these projection values it is easy to calculate the projection of the X-ray phase, and attention and scatter diffusion coefficients. However, the reconstruction of the small angle scatter distribution is more complex. Here we follow the work by Pfeiffer's group[28-31] in developing a model for dark field projections as projections of a finite set of fixed scattering directions characterizing the small angle scatter.

We assume that an X-ray beam (Fig. 1) proceeds from a spatially incoherent planar source and illuminates an irradiance distribution projected onto the object of interest. If we assume a fixed finite number of scattering directions $\epsilon_k = \zeta_k(x)\hat{\epsilon}_k \in R^3$, dark field projections of the image have the form[29]

$$d_j = \exp\left[-\int_{L_j}^{\square} \sum_k \left\langle \left| \hat{l}_j \times \hat{\epsilon}_k \right| \zeta_k(x)\hat{\epsilon}_k, t_j \right\rangle^2 dx \right] \quad , \tag{11}$$

where $\hat{l}_j \in R^3$ is the direction of the incoming beam, L_j is the line along this direction, and $t_j = |t_j|\hat{t}_j \in R^3$ is the sensitivity direction parallel to the detector surface. The $\hat{\square}$ indicates a unit vector. One can show that this reduces to

$$d_j = \exp\left[-\sum_k v_{kj} \int_{L_j}^{\square} \eta_k(x)\, dx \right],$$

where $\eta_k(x) = \zeta_k(x)^2$ and $v_{kj} = |t_j|^2 \left| \hat{l}_j \times \hat{\epsilon}_k \right|^2 \left\langle \hat{\epsilon}_k, \hat{t}_j \right\rangle^2$. The $\eta_k(x)$ at the position x are the square of the coefficients of the vector scattering directions $\hat{\epsilon}_k$.

Let's parameterize the X-ray direction so that we replace j with i, j, θ_q, ϕ_r, such that the capital letters I, J, Q, R are the dimensions for each coordinate. Defining the detector elements with coordinates (i, j) and the projection angles of the sample as θ_q, ϕ_r as shown in Fig. 1, we have dark field measurements

$$D(i, j, \theta_q, \phi_r) = \exp\left[-\sum_k v_{kijqr} \int_{L_{ijqr}}^{\square} \eta_k(x)\, dx \right]. \tag{12}$$

We can form the reconstruction problem as the solution to a large system of linear equations

$m = (m_{ijqr}) = ¿$

where $H = (D_1 A, D_2 A, \ldots, D_K A)$ is a $J \times IK$ matrix and

$$D_k = \begin{pmatrix} v_{k1111} & \cdots & 0 \\ \vdots & \ddots & \vdots \\ 0 & \cdots & v_{kIJQR} \end{pmatrix}$$

is an $IJQR \times IJQR$ diagonal matrix of weighting coefficients v_{kijqr}, $IJQR$ is the number of projection samples, NMP is the number of voxels in the 3D array, K is the number of scattering directions $\hat{\epsilon}_k$, and

$$\eta^T = (\eta_{11}, \eta_{12}, \ldots, \eta_{1NMP}, \eta_{21}, \eta_{22}, \ldots, \eta_{2NMP}, \ldots\ldots, \eta_{K1}, \eta_{K2}, \ldots, \eta_{KNMP})$$

is a $NMPK \times 1$ matrix of unknown coefficients to be determined. A is the system matrix of the tomographic projections formed by the integral in Eq. (12).

Writing the matrix formulation of the system of equations explicitly in terms of the unknown coefficients η_{ij}, we have

$$m = H\eta = \overbrace{(D_1 A, D_2 A, \ldots D_K A)}^{IJQR \times KNMP} \overbrace{\begin{pmatrix} \eta_{11} \\ ¿ \quad \vdots \\ \eta_{1NMP} \\ \eta_{21} \\ \eta_{22} \\ \vdots \\ \eta_{2NMP} \\ \vdots \\ \eta_{K1} \\ \eta_{K2} \\ \vdots \\ \eta_{KNMP} \end{pmatrix}}^{KNMP \times 1} . \tag{13}$$

In the following we will show how the pixel values with intensity $I_5(i,j)$ in Eq. (9) are related to the measurements m of the small angle scatter.

2.C. Processing phase contrast projections

As described in Section 2.A, dark field projections were simulated using an integrated wave optics framework[33,34] to model X-ray-matter interaction and free-space propagation. Our approach calculates X-ray phase contrast images formed with sources of arbitrary shape (though a plane wave was used in our simulations), and objects of preferential scattering directions. The forward model for phase contrast imaging as described in the previous section formulates the inverse problem for the reconstruction of the measured projections.

X-ray projections were simulated for an asymmetric scattering phantom in Fig. 3 consisting of four layers of parallel carbon microfibers. Each layer width was 0.5 mm and the diameter of the disk was 8 mm. The layers each consisted of an array of 71,000 fibers of 15 μm diameter. All solid carbon fibers had the same orientation along the x-axis providing preferential scatter along the y-axis perpendicular to the fibers. In our comparison of gratings and bi-prisms, for one case we performed simulations with similar gratings G_1 and G_2 both with a grating pattern width of 10.24 mm with an 8-pixel period width of 0.005 mm and grating aperture of 0.0025 mm. In the second case the G_1 and G_2 gratings were the same but G_2 was rotated by 3.6° for Moiré analysis. In the third case G_1 was replaced by an array of bi-prisms as describe in Section *2.A.4* and the G_2 grating was the same rotated grating (by 3.6°) as in the previous case.

2.C.1. Phase Stepping

The projection of the irradiance distribution onto the detector surface was approximated by fitting eight phase stepping projections to the Fourier expansion[40]

$$I_5(i,j,\theta_q,\phi_r,x_g) \approx a_0(i,j,\theta_q,\phi_r)+a_1(i,j,\theta_q,\phi_r)\cos\left[\frac{2\pi(i-(I+1)/2)}{x_p}x_g-\Phi(i,j,\theta_q,\phi_r)\right] \quad , \tag{14}$$

where (i,j) are coordinates of the detector pixel ($0 \le i \le I$); x_g is the spatial sampling in the direction of the phase grating; $x_p$is the period in x; θ_q, ϕ_r is the rotation angle of the sample around the optical axis; and a_0, a_1, and $\Phi$are the mean, amplitude, and phase of the sinusoidal curve, respectively. The definition of the visibility of the scatter and reference signal is

$$V_{obj}(i,j,\theta_q,\phi_r)=a_1^{obj}(i,j,\theta_q,\phi_r)/a_0^{obj}(i,j,\theta_q,\phi_r) \quad ,$$

$$V_{ref}(i,j,\theta_q,\phi_r)=a_1^{ref}(i,j,\theta_q,\phi_r)/a_0^{ref}(i,j,\theta_q,\phi_r) \quad .$$

The projection measurements of the small angle scatter are given as

$$m(i,j,\theta_q,\phi_r)=-\ln[D(i,j,\theta_q,\phi_r)]=-\ln\left[\frac{V_{obj}(i,j,\theta_q,\phi_r)}{V_{ref}(i,j,\theta_q,\phi_r)}\right]=-\ln\left[\frac{V_{obj}(i,j,\theta_q,\phi_r)}{V_{ref}(i,j)}\right]. \tag{15}$$

These measurements are the same as the projection of the linear diffusion coefficients. Projection of the linear attenuation coefficient is

$$p(i,j,\theta_q,\phi_r)=-\ln[T(i,j,\theta_q,\phi_r)]=-\ln\left[\frac{a_0^{obj}(i,j,\theta_q,\phi_r)}{a_0^{ref}(i,j,\theta_q,\phi_r)}\right]=-\ln\left[\frac{I_{0,obj}(i,j,\theta_q,\phi_r)}{I_{0,ref}(i,j)}\right] \quad .$$

The projection of the differential phase is

$$d_{\Phi_x}(i,j,\theta_q,\phi_r)=\frac{x_p}{\lambda D_2}\left(\Phi_{obj}(i,j,\theta_q,\phi_r)-\Phi_{ref}(i,j,\theta_q,\phi_r)\right) \quad ,$$

where x_p is the period of the phase grating, λ is the X-ray wave length, and D_2 is the distance between G_1 and G_2.

For phase stepping, we fit eight phase steps to a Fourier expansion for each projection. Then from the zero order and first order Fourier coefficients we obtain the visibility and phase of the scatter and reference signal. From this we are able to obtain the dark field projections of the small angle scatter, the projections of the linear attenuation coefficient, and the projections of the differential phase contrast.

2.C.2. Moiré fringe analysis

A Moiré pattern was superimposed on the detector irradiance distribution by rotating the G_2 grating (Fig. 1) by about 3.5833º. Both the G_1 grating and G_2 grating irradiance patterns are shown in Fig. 6. For phase stepping, the data were sampled with an image size of 16384×256, but for the Moiré pattern, the data were sampled as a 16384×16384 array. Both arrays were down sampled to 256×256.

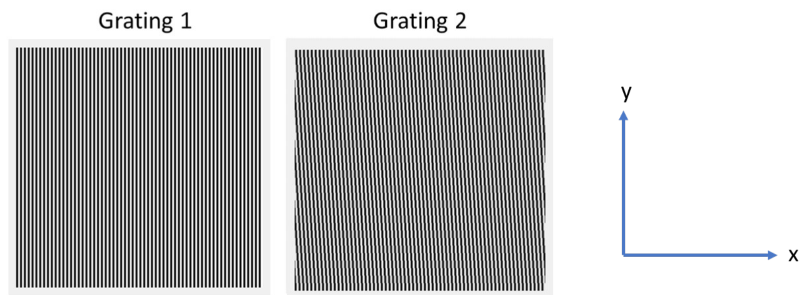

Fig. 6. A Moiré irradiance pattern was superimposed on the detector by rotating a grating by about 3.5833°. Here is an array size of 16384×16384 with pixel size of 6.25×10^{-7} m. The period of the Moiré pattern was approximately 8×10^{-5} m, twice that of the detector pixel size. The total grating pattern had a width 10.24 mm with an 8-pixel period width of 0.005 mm and grating gap of 0.0025 mm.

Each Moiré projection was processed using Fourier analysis,[13] so that the small angle scatter information encoded by the G_1 grating or bi-prism could be extracted. Three peaks related to the pattern with phantom can be observed in the Fourier transformed image in Fig. 7. A central peak (the zero harmonic) and symmetric peaks (first ordered harmonics) about the central peak, in this case just two, are observed.

Let $\left|F_n^{-1}\right|$ be the absolute value of the inverse Fourier transform (FT) around an area of the nth-order harmonic. The visibility was calculated by taking the ratio of the absolute values of the inverse FT of the area around the first-order harmonic and of the area around the zero-order harmonic: $V=\left|F_1^{-1}\right|/\left|F_0^{-1}\right|$. Then the projection of the small angle scatter, the projection of the linear attenuation coefficient, and the projection of the differential phase were calculated using

$$m(i,j,\theta_q,\phi_r) = -\ln\left[D(i,j,\theta_q,\phi_r)\right] = -\ln\left[\frac{V_{obj}(i,j,\theta_q,\phi_r)}{V_{ref}(i,j,\theta_q,\phi_r)}\right].$$

$$p(i,j,\theta_q,\phi_r) = -\ln\left[T(i,j,\theta_q,\phi_r)\right] = -\ln\left[\frac{a_0^{obj}(i,j,\theta_q,\phi_r)}{a_0^{ref}(i,j,\theta_q,\phi_r)}\right] = -\ln\left[\frac{\left|F_0^{-1}\right|_{obj}(i,j,\theta_q,\phi_r)}{\left|F_0^{-1}\right|_{ref}(i,j,\theta_q,\phi_r)}\right]$$

$$d_{\Phi_x}(i,j,\theta_q,\phi_r) = \Delta\Phi(i,j,\theta_q,\phi_r) = arg\left[F_1^{-1}\right]_{obj}(i,j,\theta_q,\phi_r) - arg\left[F_1^{-1}\right]_{ref}(i,j,\theta_q,\phi_r)$$

where $\Phi = arg\left[F_1^{-1}\right]$.

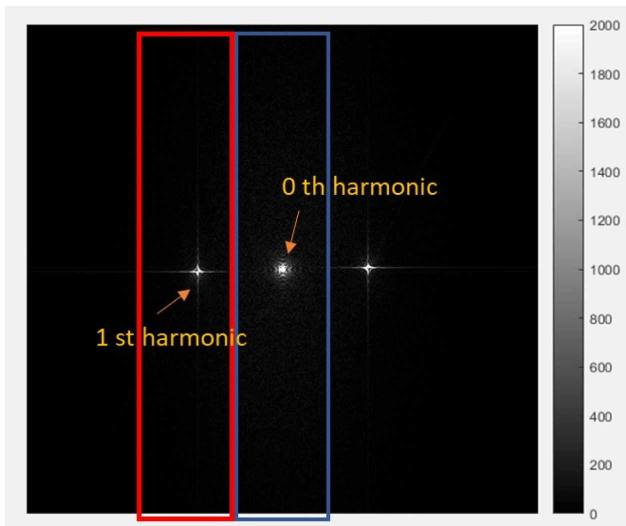

Fig. 7. Processing Moiré projections. The distance between 0th harmonic and 1st harmonic is 1/period. F_0 is obtained by centering on the central region. F_1 is obtained by centering on the region over the first harmonic peak of the FFT image.

2.E. Reconstruction of phase contrast projections

The tomographic projections of the phantom in Fig. 3 were simulated assuming parameters in Table 1. A total of 546 parallel projection images were formed for phantom rotation angles θ from 0° to 90° at 18° steps (6 angles), and ϕ from -90° to 90° at 2° steps (91 angles). Eight phase steps were used to form projections for reconstruction that were compared with reconstructions of projections formed from a single exposure Moiré pattern while G_2 grating was rotated by a small angle. The size of each projection image processed with phase stepping was 16384 × 256, which was downsampled to 256 × 256. Note that the image was oversampled along the x-scan direction to capture the small-angle scattering. The Moiré fringe analysis was performed on a single projection exposure sampled as a 16384 × 16384 array. The image was oversampled along both directions to make sure the width and length of each pixel were the same. A bi-prism was also used to replace the G_1 grating in Fig. 1 to form projections which were compared with the grating results.

The reconstructions of the vector coefficients η were performed using 25 iterations of the maximum-likelihood expectation maximization (MLEM) algorithm to maximize the likelihood function:

$$f(\eta)=L(m|\eta)=\prod_i \frac{e^{-\acute{m}_i}(\acute{m}_i)^{m_i}}{m_i!} \quad , \tag{16}$$

for measurements m in Eq. (15) with assumed mean $\acute{m}=H\eta$ in Eq. (13). The coefficient elements of vector η included $K=7$ vectors as the basis for each voxel. Every voxel was spanned by the 7-unit vectors: $[1,0,0]$, $[0,1,0]$, $[0,0,1]$, $[\sqrt{1/3},\sqrt{1/3},\sqrt{1/3}]$, $[-\sqrt{1/3},\sqrt{1/3},\sqrt{1/3}]$, $[\sqrt{1/3},-\sqrt{1/3},\sqrt{1/3}]$, $[-\sqrt{1/3},-\sqrt{1/3},\sqrt{1/3}]$. In the reconstruction the tomographic weighing factors in the projection and back projection operations were calculated on the fly for the vector reconstruction because of the large number of lines of response and lack of symmetry for storing a pre-computed weighting matrix for all vectors. A single-ray tracing method developed for GPU was used.

Apart from reconstructing the 7-vector coefficients to describe the scattering directions, we also successfully reconstructed the linear attenuation coefficients, the differential phases and the linear diffusion coefficients, which is a measure of attenuation related to small angle scattering. The three images were reconstructed separately with statistical iterative reconstruction. Ten iterations of the MLEM algorithm were implemented. The tomographic weighting factors were also calculated on the fly with single-ray tracing method.

	Simulation with Gratings	Simulation with Bi-prism and Moiré Fringe Analysis
Energy	17.5 keV	17.5 keV
Wave length λ	7.1×10^{-11} m	7.1×10^{-11} m
Wave number	1.41×10^{10}	1.41×10^{10}
Bi-prism angle χ	NA	84.624°
Bi-prism period p	NA	5 μm
Distance between phantom and G_1 D_1	0.1764 m	0.1764 m
Distance between G_1 and G_2 D_2	0.1764 m	0.1764 m
Gratings	$G_1 = G_2$	G_2 rotated 3° relative to G_1
Grating aperture	2.5 μm	2.5 μm
Grating period	5 μm	5 μm
No. Phase steps	8	1
Detector voxel size	0.04×0.04×0.04 mm^3	0.04×0.04×0.04 mm^3
Detector matrix size	256×256	256×256
Phantom circular dia.	8 mm	8 mm
Slice width	0.5 mm	0.5 mm
Fiber diameter	15 μm	15 μm
Carbon fiber index of refraction n_0	$n_0 = 1 - \delta + i\beta$ $\delta = 1.1512 \times 10^{-6}$ $\beta = 5.6117 \times 10^{-10}$	$n_0 = 1 - \delta + i\beta$ $\delta = 1.1512 \times 10^{-6}$ $\beta = 5.6117 \times 10^{-10}$
Number of fibers	71,000	71,000
No. projection angles in θ from 0° to 90° at 18° steps	6	6
No. projection angles in ϕ from -90° to 90° at 2° steps	91	91
Total No. of projection angles	546	546

Table 1. Parameters used in the simulation of the reconstruction of the phase contrast projections.

3. RESULTS

The previous sections presented our methods used to simulate the phase contrast projections of the phantom of parallel carbon microfibers. To obtain 546 projections of 284,000 fibers required 207 hours on the GPU server Dell PowerEdge R740 with two 4-core Intel(R) Xeon(R) Gold 5122 CPUs @ 3.60GHz, 128 GiB RAM, and 2 NVIDIA Tesla V100 accelerators; offering a total of 10,240 CUDA cores, 1,280 tensor cores and 16 GiB GPU RAM. In the following we present examples of the projection measurements and the reconstructions of the vector coefficients for the small angle scatter, the linear diffusion coefficient, the linear attenuation coefficient, and the differential phase.

3.A. Processing phase contrast projections

An example of one of the dark field projections is shown in Fig. 8. One sees preferential scatter oriented at approximate 45° from the vertical axis. There also appears to be some isometric scatter throughout the projection.

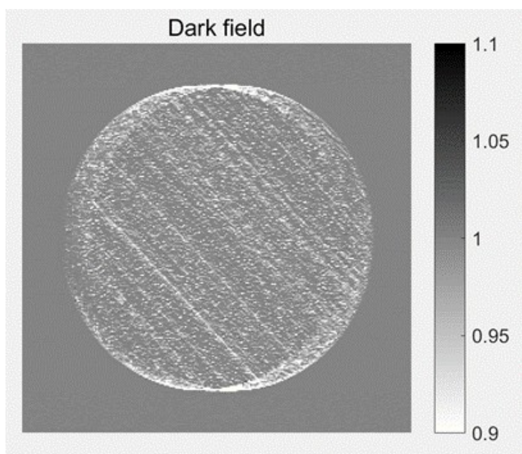

Fig. 8. Example of a dark field projection (θ = 45°, ϕ= 0°). Preferential scattering is shown rotated counterclockwise.

Figure 9 shows an example of the Moiré image obtained in the experiment. The Moiré pattern was measured both with and without the phantom.

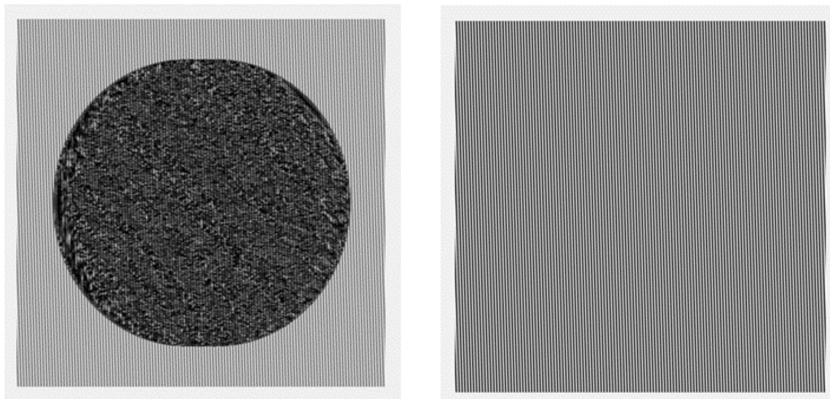

Fig. 9. Moiré pattern with (left) and without (right) phantom. The 16384×16384 arrays in the previous figure were down sampled here to 256×256.

Figure 10 gives results after taking the inverse Fourier transform of the zero and first order harmonics of the Moiré image to obtain the projection of the phantom and reference intensity and visibility. The phase of the object and reference is also presented.

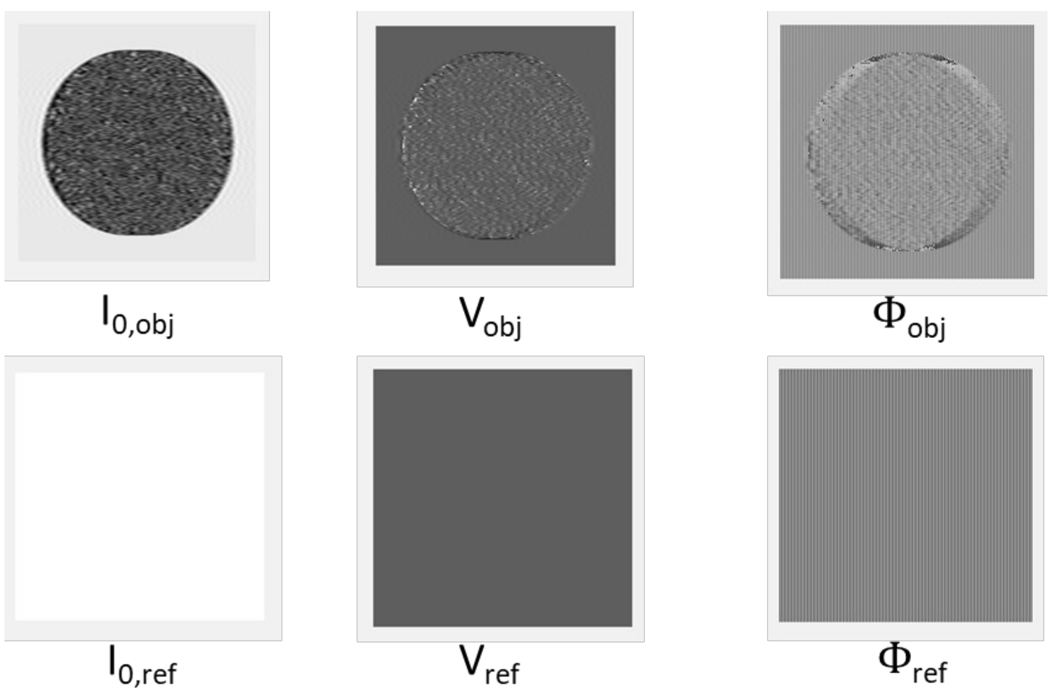

Fig. 10. Results processing Moiré projections. Left: Intensity images $I_0 = \left|F_0^{-1}\right|$ with (upper) and without (lower) the phantom. Center: Visibility images $V = \left|F_1^{-1}\right| / \left|F_0^{-1}\right|$ with and without the phantom. Right: Phase images $\Phi = arg\left(F_1^{-1}\right)$ with and without the phantom.

Figure 11 compares projections obtained by phase stepping and that obtained by Moiré fringe analysis. As expected, projections obtained by Moiré fringe analysis have more noise than phase stepping. However, the single-exposure Moiré fringe analysis takes about 1/8 the time that of phase stepping.

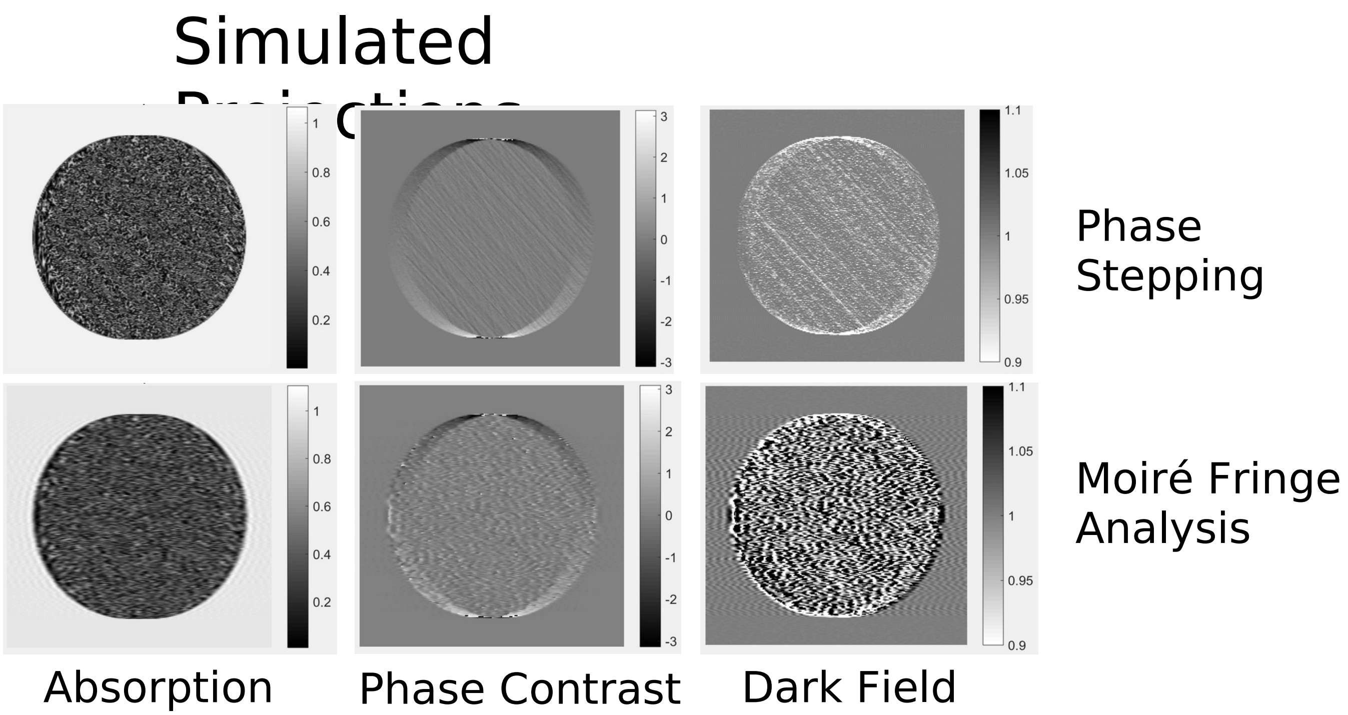

Fig. 11. Example of absorption, phase contrast, and dark field projections obtained by phase stepping (upper) and Moiré fringe analysis (lower). As expected, increased noise is observed in the Moiré dark field image.

3.B. Reconstruction of phase contrast projections

The reconstruction of the coefficients for the 7-fixed vectors in each voxel is shown in Fig. 12. Since each projection was downsampled to 256 × 256, the image matrix size was set to 256×256×256 with a voxel size of 0.04×0.04×0.04 mm^3. The image intensity in each voxel correspond to the vector amplitude. Each column from left to right are the results of grating with phase stepping, grating with Moiré fringe analysis, and bi-prism with Moiré fringe analysis. The three images across each column are the coronal (x-z plane), sagittal (y-z plane), and transaxial section (x-y plane) through the central axis of the phantom. The images going down the columns correspond to the amplitude of the 7 vectors in the sequence first starting with $[1,0,0]$, at the top and $\left[-\sqrt{1/3}, -\sqrt{1/3}, \sqrt{1/3}\right]$ at the bottom of each column.

The reconstruction results of the Moiré fringe analysis are comparable to those of phase stepping, though there is more visual noise in images of the Moiré fringe analysis. The results also show that replacing G_1 grating with bi-prism has little influence on final reconstructed results. From the reconstructed scattering vector coefficients, one can see that the maximum scattering strength is along the y-direction ([0,1,0]), which is perpendicular to the direction of the fibers and perpendicular to the sensitivity direction of the grating. Note that the third row of images for [0,0,1] in Fig. 13 are approximately zero because these are coefficients for the vector pointing along the optical axis.

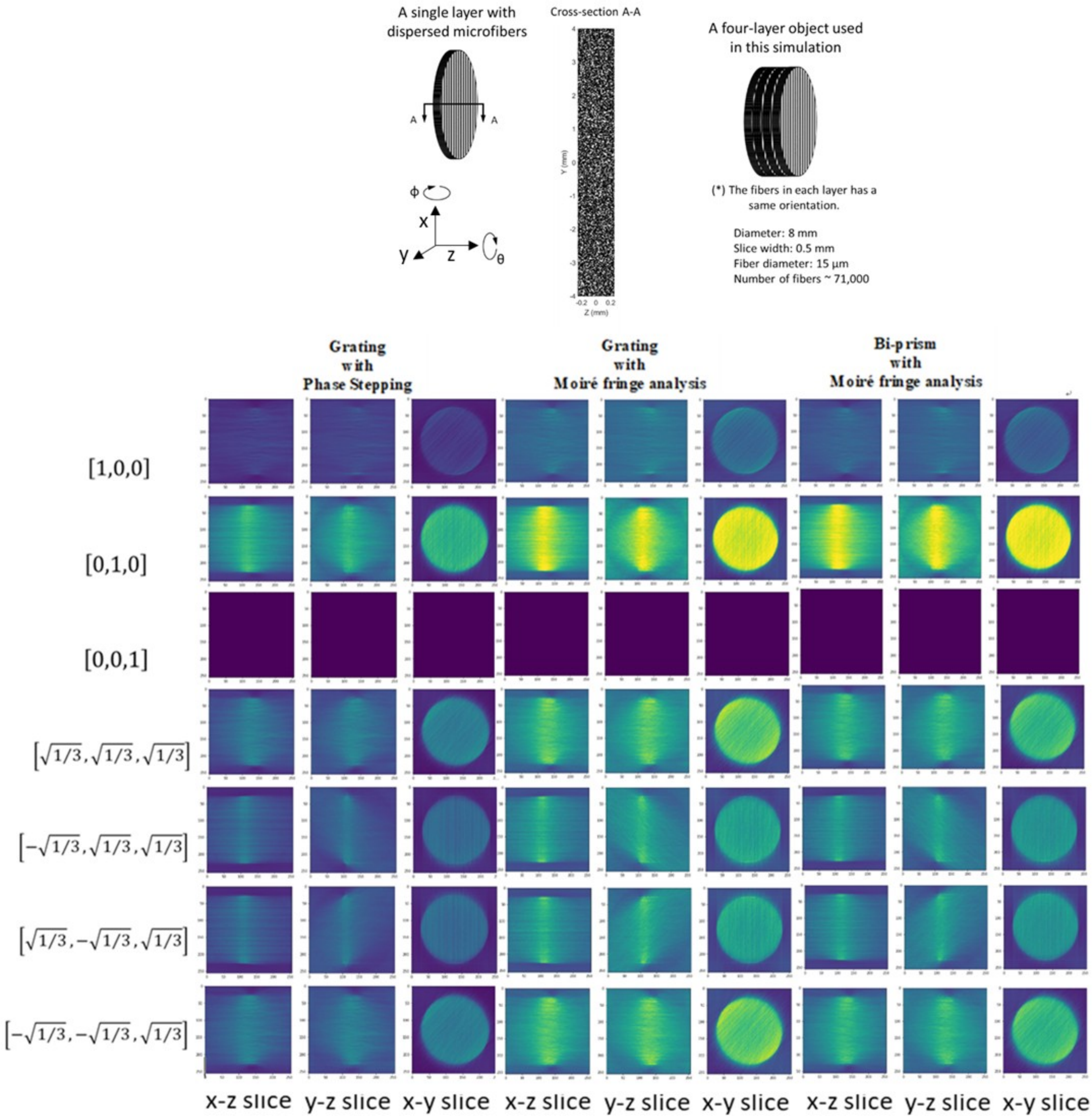

Fig. 12. Reconstructed vector coefficients from projections obtained: using grating with phase stepping (left); grating with Moiré fringe analysis (middle); bi-prism with Moiré fringe analysis (right). The three images for each at the top are the coefficients for the vector $[1,0,0]$, in the x-z slice, y-z slice, and x-y slice through the center of the phantom, respectively. The series of images from top to bottom are the coefficients for the vectors $[1,0,0]$, $[0,1,0]$, $[0,0,1]$, $[\sqrt{1/3},\sqrt{1/3},\sqrt{1/3}]$, $[-\sqrt{1/3},\sqrt{1/3},\sqrt{1/3}]$, $[\sqrt{1/3},-\sqrt{1/3},\sqrt{1/3}]$, $[-\sqrt{1/3},-\sqrt{1/3},\sqrt{1/3}]$, respectively. Note: the third row of images are zero because these are coefficients for the vector pointing along the optical axis.

Contrast to noise ratio (CNR) in Table 2 was used to evaluate the noise level of the reconstructed images. A circle with a diameter of 7.2 mm at the center was chosen as the region of interest (ROI), and a ring with an inner diameter of 9.2 mm and an outer radius of 10 mm was chosen as the background ROI. The CNR is the mean difference between the ROI and background divided by the standard derivation of the background. Table 2 lists the CNR results of the reconstructed vector coefficients for three different situations. We can see that the reconstructed coefficients with the higher visual contrast in the images (Fig. 12) also have higher CNR (Table 2). This is true for the vector coefficients of [0,1,0]. The images of the coefficients of $\left[\sqrt{1/3},\sqrt{1/3},\sqrt{1/3}\right]$ and $\left[-\sqrt{1/3},-\sqrt{1/3},\sqrt{1/3}\right]$ seem to have less contrast than those of [0,1,0], but a higher contrast (though it is subtle) than the coefficient images of $\left[-\sqrt{1/3},\sqrt{1/3},\sqrt{1/3}\right]$ and $\left[\sqrt{1/3},-\sqrt{1/3},\sqrt{1/3}\right]$. However, one would expect the contrast for [0,0,1] to be zero though the calculations from the small values give a positive CNR. From Table 2, we can see with the potential of increased fringe visibility, bi-prism interferometry can improve CNR.

Table 2 CNR of reconstructed vector coefficients

	Grating with phase stepping	Grating with Moiré fringe analysis	Bi-prism with Moiré fringe analysis
$[1,0,0]$	4.85	4.41	6.40
$[0,1,0]$	29.33	29.65	29.88
$[0,0,1]$	5.10*	5.27*	5.33*
$\left[\sqrt{1/3},\sqrt{1/3},\sqrt{1/3}\right]$	16.70	16.83	19.68
$\left[-\sqrt{1/3},\sqrt{1/3},\sqrt{1/3}\right]$	7.43	7.27	7.49
$\left[\sqrt{1/3},-\sqrt{1/3},\sqrt{1/3}\right]$	7.64	7.47	7.20
$\left[-\sqrt{1/3},-\sqrt{1/3},\sqrt{1/3}\right]$	16.51	17.98	21.29

*From Fig. 12 we see that the vector coefficients are small $\approx$ 0; however, the calculations from the small values give a positive contrast.

The reconstruction of the linear attenuation coefficient, the differential phase, and the linear diffusion coefficient from the simulation with the bi-prism are shown in Fig. 13. The image matrix size was set to 256×256×256 with a voxel size of 0.04×0.04×0.04 mm^3. The three images across each column are the coronal (x-z plane), sagittal (y-z plane) and transaxial section (x-y plane) through the central axis of the phantom.

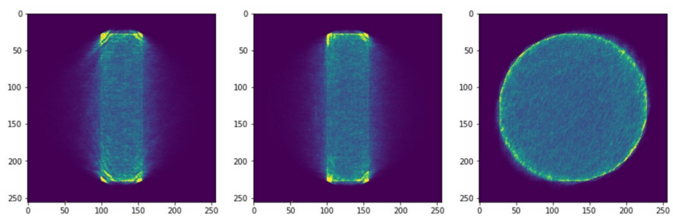

(a)

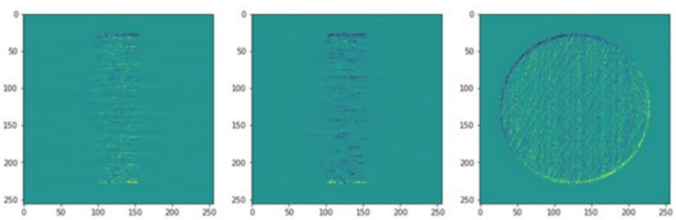

(b)

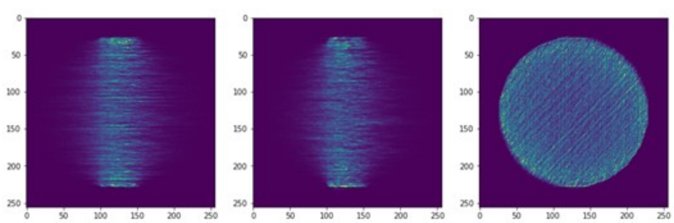

(c)

Fig. 13. Reconstructed (a) linear attenuation coefficient, (b) differential phase and (c) linear diffusion coefficient. An array of bi-prisms with Moiré fringe analysis was used to simulate these data. The three images for each are the x-z slice, y-z slice, and x-y slice through the center of the phantom, respectively.

4. DISCUSSION

This simulation study is the first to present results of the reconstruction of coefficients of a vector basis from simulated projections of X-ray small angle scatter using single-exposure Moiré fringe analysis of X-ray bi-prism interferometry projections. At every image voxel, coefficients of a fixed set of scatter vector directions are reconstructed from simulated dark field projections. Reconstructions of simulated projections using grating interferometry with phase stepping are compared with those using grating interferometry with Moiré fringe analysis and with those using bi-prism interferometry with Moiré fringe analysis. Simulations of projections are obtained using a full mathematical wave approach to X-ray refraction and diffraction assuming Rytov approximation.[36] Our projection model[28-31] of X-ray scatter compares results of grating using phase stepping with the replacement of grating by bi-prisms and single exposure Moiré fringe analysis, although with somewhat increased noise but with one eighth the acquisition time.

At every image voxel a fixed set of scatter vector directions is assumed for which the coefficients are estimated from the measured projections m in Eq. (13). Maximizing the likelihood in Eq. (16), provides estimates of these coefficients from which a tensorial representation can be obtained by fitting the weights of the fixed set of vectors to ellipsoids.[29,30] This differs significantly from reconstruction of vector and tensor fields from direct scalar measurements of projected vector and tensor fields.[45] In the present work the estimates of the coefficients were obtained by the MLEM algorithm assuming Poisson noise; however, the results show some limited angle artifacts. If angular sampling is limited as in the present case with sampling only around the $x-$¿ and $z-$¿axis, one potential solution would be to implement a compressed sensing CT reconstruction method.[48,49] For more complex samples, it may also be necessary to measure projections around the $y-$¿axis.

One of the early works to use tomography to reconstruct X-ray phase contrast data was presented by Takeda[48] and later by Bronnikov.[49] Direct Fourier analysis was used because it was recognized that the projection image of the object is modulated by the periodic grid pattern providing a strong primary peak signal around zero spatial frequency, and at least two strong harmonic peak signals centered at the periodicity of the implemented grating.[50] Iterative approaches have advantages, in addition to modeling noise, to provide constraints on the solution. Investigations along this line were pursued by Brendel *et al.*[32] who proposed a cost function with regularization to iteratively reconstruct simultaneously attenuation, phase, and scatter images (with independent penalty functions) from differential phase contrast acquisitions, without the need of phase retrieval. In another work,[51] a maximum likelihood reconstruction algorithm with regularization for differential phase contrast acquisitions was applied to sparsely sampled projections. Forward and back-projection operations were implemented using spherically symmetric basis functions (blobs).

X-ray phase contrast imaging has also been applied to non-conventional tomographic applications with the investigation of phase-contrast X-ray computed laminography[52] and tomosynthesis.[53] The specific geometry of laminography leads to unsampled frequencies in a double cone in the reciprocal space; reconstruction is improved by using prior information with an iterative filtered backprojection algorithm. For tomosynthesis,[53] the conventional attenuation image is obtained using the filtered-backprojection (FBP) algorithm with the ramp kernel; the phase contrast is reconstructed using FBP with a Hilbert kernel; whereas, the differential phase contrast image is reconstructed by removing differentiation operator in the equation involving the Hilbert kernel because of the differential nature in the differential phase contrast projections.

In our previous work,[45,59,60] we mathematically represent tensor tomography as the direct reconstruction of elements of a rank-2 tensor $T(x)$ from 3D directional X-ray projections of $T(x)$ defined by

$p^{\theta\tau}(\underline{s};\underline{\theta}) = \int_R \underline{\theta}^T T(\underline{s}+l\,\underline{\theta})\,\underline{\tau}\,dl$, where $\underline{\theta}$, $\underline{\tau}$ are three-dimensional directional unit vectors; or of elements of a rank-1 tensor (vector) $v(x)$ defined by $p^{\theta}(\underline{s};\underline{\theta})=\int_{R} \underline{\theta}^{T} v(\underline{s}+l\,\underline{\theta})\,dl$. The algorithms involve reconstructing directly the elements of the tensor or vector.

The tensor tomography algorithms of Pfeiffer's group[28-31] did not directly reconstruct elements of a second order tensor or of a first order tensor (vector field). Their X-ray tensor tomography (XTT) method[28] involved a two-step process of reconstructing coefficients of a Cartesian vector basis at each voxel and then fitting that to an ellipsoidal representation of the tensor at each voxel. The forward model was an ingenious representation of small angle scatter as the discrete supposition of the anisotropic scatter signal, much like the Beer–Lambert model for the X-ray attenuation signal.[31] Vogel et al.[29] formulated the reconstruction of the ellipsoidal representation as a regular inverse problem [see Eq. (13)] whereby an iterative reconstruction algorithm is used to estimate vector coefficients constrained by an ellipsoidal function. Later Wieczorek et al.[56] developed what they termed anisotropic X-ray dark field tomography (ANDT), modifying the previous algorithm by replacing the Cartesian vector representation of the scatter in each voxel by a spherical harmonic expansion. Redefining the forward model for the spherical function representation of the small angle scatter, a reconstruction algorithm was developed whereby coefficients of the spherical harmonics were estimated to represent the reconstruction of the multiple scattering directions within single voxels. They demonstrated that the rank-2 tensor model of XTT[28,31] is a special case of this continuous model.

The first tensor tomography approach to directly reconstruct elements of a second rank tensor representation of small angle scatter from dark field projections was presented by Gao *et al.*[58] They modeled the projection of a rank-2 symmetric tensor distribution of the anisotropic scatter in every voxel as the scalar measure of the product of a symmetric 3×3 tensor matrix $T(x)$ with two equal unit vectors $\underline{\tau}$ orthogonal to the incoming X-ray beam $\underline{\theta}$: $p^{\tau\tau}(\underline{s};\underline{\theta})=\int_{R} \underline{\tau}^{T} T(\underline{s}+l\,\underline{\theta})\,\underline{\tau}\,dl$. The tensor tomographic reconstruction was performed by what they termed an iterative reconstruction tensor tomography (IRTT) algorithm, which used an iterative method similar to ART[61] to minimize the difference between the forward model and the measured data. The IRTT algorithm was used to demonstrate the reconstruction of nanostructure anisotropy of a carbon fiber knot, a human bone trabecula specimen, and a fixed mouse brain. The paper did an extensive comparison with their IRTT method and the small-angle X-ray scattering tensor tomography (SASTT) reconstruction method,[54,55] both in comparison of the theory and results, indicating that the reconstruction speed for the IRTT was faster than that of the SASTT reconstruction method. The SASTT method uses spherical harmonics in fitting the three-dimensional reciprocal-space map for each voxel. A more general reciprocal-space formulation was developed by Schaff et al.[57] who proposed an algorithm where *a posteriorly* virtual axes of rotation are interrogated for the 3D reciprocal-space momentum vector q to find the projection angles and 2D scattering orientations that would align to the virtual axis. Several virtual axes are analyzed for each voxel to obtain the best fit for q. This requires a dense sampling of projections to identify the rotationally invariant component of the scatter in each voxel.

What is missing in these methods is tomographic data sufficiency conditions required to uniquely reconstruct the tensor components. We know from the works of Desai and Lionheart[62] that the 6 unknown tensor components can be uniquely reconstructed by sampling special protection measurements, which are projections of a subspace of the 3D tensor field around 3-orthogonal axes. Still, more work is needed in the tensor reconstruction of phase contrast interferometry data to verify the uniqueness of the solution and devising methods of uniquely reconstructing tensors from phase contrast interferometry.

5. CONCLUSION

Our simulations of anisotropic X-ray dark-field imaging of a phantom consisting of parallel carbon microfibers show an advantage of bi-prism X-ray interferometry with Moiré fringe analysis over X-ray grating interferometry with phase stepping. This advantage is pronounced for certain scattering vectors and is due to the expected increase in fringe visibility using a bi-prism interferometer.

Future work will investigate the use of a detector/scintillator with small hexagonal elements to provide the Moiré patterns.[26,27]

ACKNOWLEDGEMENTS

This work was supported in part by the National Institutes of Health under Grant Nos. R43 EB027535, R01 EB026332, R01 HL135490, and China Scholarship Council Grant No. 201906230215. We also gratefully acknowledge the support of NVIDIA Corporation with the donation of a Quadro P6000 GPU and the University of Wisconsin-Milwaukee High Performance Computing facility for providing the computer time on the GPU cluster.

CONFLICT OF INTEREST

The authors have no conflict of interest.

References

1. Pfeiffer F, Bunk O, David C, Bech M, Duc GL, Bravin A, Cloetens P, High resolution brain tumor visualization using three-dimensional x-ray phase contrast tomography. *Phys Med Biol*. 2007;52:6923-6930.

2. Doblas A, Saavedra G, Martinez-Corral M, Barreiro JC, Sanchez-Ortiga E, Llavador A, Axial resonance of periodic patterns by using a Fresnel biprism. *J Opt Soc Am A*. 2013;30:140-148.

3. Ablett JM, Evans-Lutterodt K, Stein A, Hard x-rays Fresnel prisms: Properties and applications, in Design and Microfabrication of Novel X-ray Optics II, A. A. Snigirev and D. C. Mancini, Eds. Proceedings of SPIE, vol. 5539, August 2, 2004.

4. Gullberg GT, Fuller M, Shrestha U, Seo Y, Tensor tomography of dark field scatter using x-ray interferometry with bi-prisms. 2017 IEEE Nuclear Science Symposium and Medical Imaging Conference Record (NSS/MIC), Oct. 21 – 28, 2017, Atlanta, Georgia.

5. Bonse U, Hart M, An x-ray interferometer. *Appl Phys Lett.* 1965;6(8):155.

6. Clauser JF, Reinsch ME, New theoretical and experimental results in Fresnel optics with applications to matter-wave and x-ray interferometry. *Appl Phys B*. 1992;54(5):380–95.

7. Momose A, Kawamoto S, Koyama I, Hamaishi Y, Takai K, Suzuki Y, Demonstration of X-ray Talbot interferometry. *Jpn J Appl Phys.* 2003;42:L866–8.

8. David C, Nöhammer B, Solak HH, Differential x-ray phase contrast imaging using a shearing interferometer. *Appl Phys Lett*. 2002;81:3287.

9. Liu H, Cartwright AN, Basaran C, Sensitivity improvement in phase shifted moiré interferometry using 1D continuous wavelet transform image processing. *Opt Eng.* 2003;42:2646–52.

10. Liu H, Cartwright AN, Basaran C, Moiré interferogram phase extraction: A ridge detection algorithm for continuous wavelet transforms. *Appl Opt*. 2004;43(41):850-857.

11. Weitkamp T, Diaz A, David C, Pfeiffer F, Stampanoni M, Cloetens P, Ziegler E, X-ray phase imaging with a grating interferometer. *Opt Express.* 2005;13:6296–304.

12. Pfeiffer F, Weitkamp T, Bunk O, David C, Phase retrieval and differential phase-contrast imaging with low-brilliance X-ray sources. *Nat Phys.* 2006;2:258–61.

13. Seifert M, Gallersdörfer M, Ludwig V, Schuster M, Horn F, Pelzer G, Rieger J, Michel T, Anton G, Improved reconstruction technique for Moiré imaging using an X-ray phase-contrast Talbot–Lau interferometer. *J Imaging*. 2018;4(62):68-81.

14. Suzuki Y, Takeuchi A, Hard x-ray holographic microscopy using refractive prism and Fresnel zone plate objective. *Rev Sci Instrum.* 2005;76:093702.

15. Isakovic F, Stein A, Warren JB, Sandy AR, Narayanan S, Sprung M, Ablett JM, Siddons DP, Metzler M, Evans-Lutterodt K, A bi-prism interferometer for hard X-ray photons. *J Synchrontron Radiat*. 2010;17:451-5.

16. Zverev D, Snigireva I, Kohn V, Kuznetsov S, Yunkin V, Snigirev A, X-ray phase-sensitive imaging using a bilens interferometer based on refractive optics. *Opt Express* 2020;28(15):21856.

17. Lang AR, Makepeace APW, Production of synchrotron x-ray biprism interference patterns with control of fringe spacing. *J Synchrotron Rad*. 1999;6:59–61.

18. Jacques V, Wu E, Toury T, Treussart F, Aspect A, Grangier P, Roch J-F, Single-photon wavefront-splitting interference: An illustration of the light quantum in action. *Eur Phys J D* 2005;35:561–565.

19. Jacques V, Lai ND, Dréau A, Zheng D, Chauvat D, Treussart F, Grangier P, Roch J-F, Illustration of quantum complementarity using single photons interfering on a grating. *New J Phys*. 2008;10:123009.

20. Missiroli GF, Pozzi G, Valdri U, Electron interferometry and interference electron microscopy. *J Phys E Sci Instrum*. 1981;14:649–71.

21. Bennett EE, Kopace R, Stein AF, Wen H, A grating-based single-shot x-ray phase contrast and diffraction method for *in vivo* imaging. *Med Phys.* 2010;37:6047-6054.

22. Bevins N, Zambelli J, Li K, Qi Z, Multicontrast x-ray computed tomography imaging using Talbot-Lau interferometry without phase stepping. *Med Phys.* 2012:39:424-428.

23. Marschner M, Willner M, Potdevin G, Fehringer A, Noël PB, Pfeiffer F, Herzen J, Helical X-ray phase-contrast computed tomography without phase stepping. *Sci Rep*. 2016;6:23953.

24. Itoh H, Nagai K, Sato G, Yamaguchi K, Nakamura T, Kondoh T, Ouchi C, Teshima T, Setomoto Y, Den T, Two-dimensional grating-based X-ray phase-contrast imaging using Fourier transform phase retrieval. *Opt Express.* 2011;19(4):3339-46.

25. Miao H, Panna A, Gomella AA, Bennett EE, Znati S, Chen L, Wen H, A universal moiré effect and application in X-ray phase-contrast imaging. *Nat Phys.* 2016;12:830–4.

26. Sahlholm A, Svenonius O, Petersson S, Scintillator technology for enhanced resolution and contrast in X-ray imaging. *Nuclear Instruments and Methods in Physics Research Section A: Accelerators, Spectrometers, Detectors and Associated Equipment.* 2011;648:S16-S19.

27. Rutishauser S, Zanette I, Donath T, Sahlholm A, Linnros J, David C, Structured scintillator for hard x-ray grating interferometry. *Appl Phys Lett*. 2011;98(17):171107 - 171107-3.

28. Malecki A, Potdevin G, Biernath T, Eggl E, Willer K, Lasser T, Maisenbacher J, Gibmeier J, Wanner A, Pfeiffer F, X-ray tensor tomography. *EPL* (Europhysics Letters), 2014;105(3):38002.

29. Vogel J, Schaff F, Fehringer A, Jud C, Wieczorek M, Pfeiffer F, Lasser T, Constrained X-ray tensor tomography. *Opt Express*. 2015 ;23:15134-51.

30. Sharma Y, Wieczorek M, Schaff F, Seyyedi S, Prade F, Pfeiffer F, Lasser T, Six dimensional X-ray tensor tomography with a compact laboratory setup. *Appl Phys Lett.* 2016;109:134102.

31. Malecki AD, X-ray Tensor Tomography. Ph.D. Thesis. Technical University of München, August, 2013.

32. Brendel B, von Teuffenbach M, Noël PB, Pfeiffer F, Koehler T, Penalized maximum likelihood reconstruction for x-ray differential phase-contrast tomography. *Med Phys.* 2016;43(1):188.

33. Paganin DM, Coherent X-ray Optics, Oxford University Press, New York, NY, 2013.

34. Goodman JW, Introduction to Fourier Optics (Third Edition), Roberts & Company, Englewood, Colorado, 2005.

35. Sung Y, Sheppard CGR, Barbastathis G, Ando M, Gupta R, Full-wave approach for x-ray phase imaging. *Opt Express*. 2013;21:266–77.

36. Sung Y, Barbastathis G, Rytov approximation for x-ray phase imaging. *Opt Express.* 2013;21:2674–82.

37. Sung Y, Segars WP, Pan A, Ando M, Sheppard CGR, Gupta R, Realistic wave-optics simulation of X-ray phase-contrast imaging at a human scale. *Sci Rep.* 2015;5:12011.

38. Shanblatt ER, Sung Y, Gupta R, Nelson BJ, Leng S, Graves WS, McCollough CH, Forward model for propagation-based x-ray phase contrast imaging in parallel- and cone-beam geometry. *Opt Express*, 2019;27(4):4504.

39. Sung Y, Nelson B, Shanblatt ER, Gupta R, McCollough CH, Graves WS, Wave-optics simulation of grating-based X-ray phase-contrast imaging using 4D Mouse Whole Body (MOBY) phantom. *Med Phys,* 2020;47(11):5761-71.

40. Jensen TH, Bech M, Bunk O, Donath T, David C, Feidenhans lR, Pfeiffer F, Directional x-ray dark-field, imaging. *Phys Med Biol*. 2010;55:3317-23.

41. Yashiro W, Terui Y, Kawabata K, Momose A, On the origin of visibility contrast in X-ray Talbot interferometry. *Opt Express.* 2010;18:16890–901.

42. Kitchen MJ, Paganin D, Lewis RA, Yagi N, Uesugi K, Mudie ST, On the origin of speckle in X-ray phase contrast images of lung tissue. *Phys Med Biol.* 2004;49:4335.

43. Malecki A, Potdevin G, Pfeiffer F, Quantitative wave-optical numerical analysis of the dark-field signal in grating-based x-ray interferometry. *Europhys Lett*. 2012;99(4):48001.

44. Shanblatt ER, Sung Y, Gupta R, Nelson BJ, Leng S, Graves WS, McCollough CH, Forward model for propagation-based x-ray phase contrast imaging in parallel- and cone-beam geometry. *Opt Express*, 2019;27(4):4504.

45. Gullberg GT, Ghosh Roy D, Zeng GL, Alexander AL, Parker DL, Tensor tomography. *IEEE Trans on Nucl Sci.* 1999;46:991-1000.

46. Bao p, Xia W, Yang K, Chen W, Chen M, Xi Y, Niu S, Zhou J, Zhang H, Sun H, Wang Z, Zhang Y, Convolutional sparse coding for compressed sensing CT reconstruction, *IEEE Trans Med Imag*, 2019;38:2607-19.

47. Sidky EY, Pan X, Image reconstruction in circular cone-beam computed tomography by constrained, total-variation minimization, *Phys Med Biol.* 2008:53:4777–4807.

48. Takeda M, Ina H, Kobayashi S, Fourier-transform method of fringe-pattern analysis for computer-based topography and interferometry. *J Opt Soc Am*. 1982; 72:156–60.

49. Bronnikov AV, Theory of quantitative phase-contrast computed tomography. *J Opt Soc Am A*. 2002;19(3):472-80.

50. Wen H, Bennett EE, Hegedus MM, Carroll SC, Spatial harmonic imaging of X-ray scattering--initial results. *IEEE Trans Med Imaging*. 2008;27(8):997-1002.

51. Köhler T, Brendel B, Roessl E, Iterative reconstruction for differential phase contrast imaging using spherically symmetric basis functions. *Med Phys.* 2011;38(8):4542-5.

52. Harasse S, Yashiro W, Momose A, Iterative reconstruction in x-ray computed laminography from differential phase measurements. *Opt Express.* 2011;19(17):16560-73.

53. Li K, Ge Y, Garrett J, Bevins N, Zambelli J, Chen G, Grating-based phase contrast tomosynthesis imaging: Proof-of-concept experimental studies. *Med Phys.* 2014;41(1):011903.

54. Liebi M, Georgiadis M, Menzel A, Schneider P, Kohlbrecher J, Bunk O, Guizar-Sicairos M, Nanostructure surveys of macroscopic specimens by small-angle scattering tensor tomography. *Nature*. 2015;527(7578):349-52.

55. Liebi M, Georgiadis M, Kohlbrecher J, Holler M, Raabe J, Usov I, Menzel A, Schneider P, Bunk O, Guizar-Sicairos M, Small-angle X-ray scattering tensor tomography: Model of the three-dimensional reciprocal-space map, reconstruction algorithm and angular sampling requirements *Acta Crystallogr A Found Adv*. 2018;74(Pt 1):12-24.

56. Wieczorek M, Schaff F, Pfeiffer F, Lasser T: Anisotropic X-ray dark-field tomography: A continuous model and its discretization, *Phys. Rev. Lett*. 117, 158101, 2016.

57. Schaff F, Bech M, Zaslansky P, Jud C, Liebi M, Guizar-Sicairos M, Pfeiffer F, Six-dimensional real and reciprocal space small-angle X-ray scattering tomography. *Nature*, 2015;527:353–6.

58. Gao Z, Guizar-Sicairos M, Lutz-Bueno V, Schröter A, Liebi M, Rudin M, Georgiadis M, High-speed tensor tomography: Iterative reconstruction tensor tomography (IRTT) algorithm. *Acta Cryst.* 2019;A75:223–38.

59. Panin VY, Zeng GL, Gullberg GT, Regularized iterative reconstruction in tensor tomography using gradient constraints. *IEEE Trans on Nucl Sci*. 2002;49:2387-93.

60. Cheryauka AB, Lee JN, Samsonov AA, Defrise M, Gullberg GT, MRI diffusion tensor reconstruction with PROPELLER data acquisition. *Magn Reson Imag*. 2004;22:139-48.

61. Gordon R, Bender R, Herman GT, Algebraic reconstruction techniques (ART) for three-dimensional electron microscopy and x-ray photography. *J Theor Biol*. 1970;29:471-81.

62. Desai NM, Lionheart WRB, An explicit reconstruction algorithm for the transverse ray transform of a second rank tensor field from three axis data. *Inverse Problems* 2016;32:115009.

FIGURE CAPTIONS

Fig. 1. Schematic diagram of the X-ray bi-prism interferometry system used in our simulations. An X-ray tube produces multiple X-rays passing through a source grating G_0. The source grating forms multiple coherent but mutually incoherent sources of X-rays. These refract or diffract through the G_1 grating (either bi-prism or binary grating in our simulations) and are scattered by the object. The resultant X-rays pass through an analyzing grating G_2 (either phase stepping grating or a rotated grating for Moiré fringe analysis in our simulations). In Section 2.B, we present the imaging model. For this model, the following unit vectors: $\hat{\epsilon}_1, \hat{\epsilon}_2, \hat{\epsilon}_3 \in R^3$ are three scattering directions [in our simulations we used 7 scattering directions $(K=7)$], $\hat{l}_j \in R^3$ is the direction of the incoming X-ray beam, and $\hat{t}_j \in R^3$ is the sensitivity direction parallel to the detector surface.

Fig. 2. (a) Density plot of a fringe visibility pattern for 25-point sources with 1 bi-prism. The amplification of the interference pattern is repeated at non-periodic distances away from the plane of the bi-prism. For the calculation we set $\lambda=7.1\times10^{-11}$ m (17.5 keV), $I_p=1/\Delta^2$, $\Delta=7.00\times10^{-7}$ m, $\alpha=\delta\tan(\chi)$, $\delta=1.57\times10^{-6}$ (silicon), $\chi=82°$, $\eta=0.4$ m, and $x_0=36.7\,\mu$m. (b) Talbot-Lau carpet. Illuminating plane wave passes through a grating producing a fringe pattern with replicating amplified fringe patterns at regular distances from the sources produced by the grating. At $z_T/2$ there is a secondary Talbot image and at z_T a replication of the original Talbot image that emerged from the grating. At $z_T/4$ there is a double frequency fractional image and increased frequency of images at less fractional distances. (Modified from Wikipedia: https://en.wikipedia.org/wiki/Talbot_effect.)

Fig. 3. Phantom used in the simulations. The phantom consisted of four layers of parallel carbon microfibers to provide preferential scatter perpendicular to the direction of the fibers. The angles ϕ and θ show the rotation directions of the projections of the phantom.

Fig. 4. Schematic diagram of the simulation geometry used in the simulation study. G_1 and G_2 are the gratings and the phantom is the four layers of fibers shown in Fig. 3. D_1 is the distance between the phantom and the first grating G_1. D_2 is the distance between the first grating and the second grating G_2. The numbers 1 through 5 in the circles refer to the planes where Eqs. (5)-(9) were calculated. For the phase grating simulation, the phase grating G_2 was shifted 8 positions in the y-direction over one period. For the Moiré simulation G_2 was rotated by 3°. (This figure was modified from Fig. 1 in Sung *et al.*[39])

Fig. 5. Bi-prism replaces the binary grating in G_1 for the simulations. This results in a trapezoidal phase shift along the x-direction, which can be represented as $\phi(x)=\Lambda(x)*\Pi(x)$.

Fig. 6. A Moiré irradiance pattern was superimposed on the detector by rotating a grating by about 3.5833°. Here is an array size of 16384×16384 with pixel size of 6.25×10^{-7} m. The period of the Moiré pattern was approximately 8×10^{-5} m, twice that of the detector pixel size. The total grating pattern had a width 10.24 mm with an 8-pixel period width of 0.005 mm and grating gap of 0.0025 mm.

Fig. 7. Processing Moiré projections. The distance between 0th harmonic and 1st harmonic is 1/period. F_0 is obtained by centering on the central region. F_1 is obtained by centering on the region over the first harmonic peak of the FFT image.

Fig. 8. Example of a dark field projection (θ = 45°, ϕ=0°). Preferential scattering is shown rotated counterclockwise.

Fig. 9. Moiré pattern with (left) and without (right) phantom. The 16384×16384 arrays in the previous figure were down sampled here to 256×256.

Fig. 10. Results processing Moiré projections. Left: Intensity images $I_0 = \left|F_0^{-1}\right|$ with (upper) and without (lower) the phantom. Center: Visibility images $V = \left|F_1^{-1}\right| / \left|F_0^{-1}\right|$ with and without the phantom. Right: Phase images $\Phi = arg\left(F_1^{-1}\right)$ with and without the phantom.

Fig. 11. Example of absorption, phase contrast, and dark field projections obtained by phase stepping (upper) and Moiré fringe analysis (lower). As expected, increased noise is observed in the Moiré dark field image.

Fig. 12. Reconstructed vector coefficients from projections obtained: using grating with phase stepping (left); grating with Moiré fringe analysis (middle); bi-prism with Moiré fringe analysis (right). The three images for each at the top are the coefficients for the vector $[1,0,0]$, in the x-z slice, y-z slice, and x-y slice through the center of the phantom, respectively. The series of images from top to bottom are the coefficients for the vectors $[1,0,0]$, $[0,1,0]$, $[0,0,1]$, $[\sqrt{1/3}, \sqrt{1/3}, \sqrt{1/3}]$, $[-\sqrt{1/3}, \sqrt{1/3}, \sqrt{1/3}]$, $[\sqrt{1/3}, -\sqrt{1/3}, \sqrt{1/3}]$, $[-\sqrt{1/3}, -\sqrt{1/3}, \sqrt{1/3}]$, respectively. Note: the third row of images are zero because these are coefficients for the vector pointing along the optical axis.

Fig. 13. Reconstructed (a) linear attenuation coefficient, (b) differential phase and (c) linear diffusion coefficient. An array of bi-prisms with Moiré fringe analysis was used to simulate these data. The three images for each are the x-z slice, y-z slice, and x-y slice through the center of the phantom, respectively.